Multimodal synchrotron x-ray diffraction across the superconducting transition of $Sr_{0.1}Bi_2Se_3$

M. P. Smylie,[1,2] Z. Islam,[3] A. Glatz,[1,4] G. D. Gu,[5] J. A. Schneeloch,[5] R. D. Zhong,[5] S. Rosenkranz,[1] W.-K. Kwok,[1] and U. Welp[1]

[1]*Materials Science Division, Argonne National Laboratory, 9700 S. Cass Avenue, Lemont, Illinois 60439, USA*
[2]*Department of Physics and Astronomy, Hofstra University, Hempstead, New York 11549, USA*
[3]*Advanced Photon Source, Argonne National Laboratory, Lemont, Illinois 60439, USA*
[4]*Department of Physics, Northern Illinois University, DeKalb, Illinois 60115, USA*
[5]*Condensed Matter Physics and Materials Science Department, Brookhaven National Laboratory, Upton, New York 11793, USA*

(Received 27 July 2022; revised 27 May 2024; accepted 27 June 2024; published 17 July 2024)

In the doped topological insulator $Sr_xBi_2Se_3$, a pronounced in-plane twofold symmetry is observed in electronic properties below the superconducting transition temperature $T_c \sim 3$ K, despite the threefold symmetry of the observed $R\bar{3}m$ space group. The axis of twofold symmetry is nominally pinned to one of three rotationally equivalent crystallographic directions and crystallographic strain has been proposed to be the origin of this pinning. We carried out multimodal synchrotron diffraction and resistivity measurements down to ~0.68 K and in magnetic fields up to 45 kG on a single crystal of $Sr_xBi_2Se_3$ to probe the effect of superconductivity on the crystallographic distortion. Our results indicate that there is no in-plane crystallographic distortion at the level of 1×10^{-5} associated with the superconducting transition. These results further support the model that the large twofold in-plane anisotropy of superconducting properties of $Sr_xBi_2Se_3$ is not structural in origin, but electronic, namely, it is caused by a nematic superconducting order parameter of E_u symmetry.

DOI: 10.1103/PhysRevB.110.024509

I. INTRODUCTION

Following the discovery of topological insulators [1–5], with an insulating gap in the bulk and a gapless conductive surface state, it was quickly realized [6–14] that the superconducting version, the topological superconductor, could exist. A topological superconductor can have a nodeless or nodal superconducting gap in the bulk, [15], while simultaneously possessing gapless surface states. These surface states may support quasiparticle excitations which are Majorana zero modes whose non-Abelian nature could be used to create a robust quantum computer [16–18]. Two methods have been used to generate topological superconductivity: (1) via the proximity effect [19–23] by deposition of a conventional *s*-wave superconductor onto a topological insulator surface and (2) via doping a topological insulator [24–28] to evoke bulk superconductivity. The former approach has shown great promise, but definitive Majorana detection remains controversial [29,30]. The latter method has revealed some unexpected electronic behavior.

Doping with either Cu, Nb, or Sr [25,31,32] induces superconductivity in the well-known topological insulator Bi_2Se_3 [5], while preserving its topological order [33]; doping with Fe has also recently been reported to generate superconductivity [34]. The first observation of superconductivity was reported in $Cu_xBi_2Se_3$ [25] with a T_c of ~3.4 K and a full superconducting gap [35]. However, this material is not air stable and reported superconducting volume fractions in single crystals are typically low [25,36–38]. $Nb_xBi_2Se_3$ has a similar $T_c \sim 3.4$ K, albeit the synthesis of this material remains challenging [39–44]. In particular, an unresolved issue for Cu and Nb doping is the determination of the exact location of the dopant ions in the superconductor. Recent reports [43,45–49] yield conflicting results as to whether the dopant ions are intercalated in the van der Waals gap, are incorporated in other locations in the lattice, or undergo clustering [50]. Quantum oscillation measurements on Nb-doped Bi_2Se_3 [51] indicate multiple Fermi surface sheets, and penetration depth [52,53] and scanning tunneling microscopy (STM) measurements [50] find a nodal superconducting gap structure. Sr doping [32], on the other hand, generates superconductivity at $T_c \sim 3.0$ K, and millimeter-scale stable crystals can be grown with nearly 100% superconducting volume fraction [54,55]. STM measurements [56] suggest a full superconducting gap. In the Cu- and Sr-doped compounds, quantum oscillations and angle-resolved photoemission spectroscopy (ARPES) measurements [32,57–60] show only one cylindrical Fermi surface sheet, and for $Cu_xBi_2Se_3$, the Fermi surface is found to undergo a Lifshitz transition from closed ellipsoidal to an open warped cylindrical Fermi surface [59,61] upon sufficient doping to elicit superconductivity.

All three compounds with Cu, Nb, and Sr doping share the same $R\bar{3}m$ trigonal structure of the parent compound Bi_2Se_3. Therefore, the observation of a pronounced twofold in-plane asymmetry of the superconducting state is unexpected [62]. First observed in Knight shift measurements on $Cu_xBi_2Se_3$ [63], this behavior was interpreted as signature of odd-parity superconductivity [64]. Subsequently, a pronounced twofold basal plane symmetry was observed in magnetoresistivity, calorimetry, torque magnetometry, and upper critical field measurements [62,65–69] in the superconducting state of the three Bi_2Se_3-derived compounds $Cu_xBi_2Se_3$, $Nb_xBi_2Se_3$, and $Sr_xBi_2Se_3$ despite their threefold symmetric crystal structure. STM measurements [70] directly show a twofold

symmetric superconducting gap in $Cu_xBi_2Se_3$. A pseudospin triplet, nematic superconducting state with a two-component order parameter has been proposed [64,71] to account for the observed twofold symmetry below T_c. This state is odd parity and has E_u symmetry and allows for the possibility of an anisotropic full gap as well as a nodal gap. Either gap structure qualifies as topological [15], and the observation of zero-bias conductivity peaks in spectroscopy measurements [72–74] has been interpreted as a signature of Majorana states on the surface. While the uncertainties regarding the microstructure of doped superconducting Bi_2Se_3-derived materials mentioned above pose challenges in clarifying the nature of the superconducting state, the observation of the twofold superconducting anisotropy in the field-angle-dependent specific heat of $Sr_{0.1}Bi_2Se_3$ [68] shows that it is a bulk phenomenon, not caused by interfaces or minority phases. This rotational symmetry-breaking state and its observed insensitivity to disorder [53,75–77] would identify the doped Bi_2Se_3 superconductors as a new type of unconventional superconductor, as both the gap amplitude and phase are lower symmetry than that of the lattice.

Theoretical models predict that the nematic director is aligned with either the a or the a^* direction in the crystal. As each has three rotationally equivalent directions due to the threefold symmetry in the $R\bar{3}m$ structure, the appearance of three equivalent nematic domains is expected to preserve the overall symmetry of the $R\bar{3}m$ structure. However, the majority of experimental reports show a single nematic axis accompanied by a pronounced twofold in-plane anisotropy. We have previously observed the nematic axis to be pinned to one particular in-plane a axis. For a given crystal, this axis does not change upon repeated thermal cycling to room temperature. A nematic axis along the a axis is consistent with the proposed nodal $\Delta 4_x$ state. However, other groups have reported [78,79] crystals with a^* pinning, consistent with the proposed anisotropic but fully gapped $\Delta 4_y$ state. One report presents angular-dependent magnetotransport data on a uniaxially strained single crystal [80] which revealed a redistribution of the three rotationally equivalent nematic axis configurations with strain. Theoretical models [71,81,82] predict that the superconducting order parameter couples linearly to strain fields, thereby providing a mechanism for the selection of a nematic axis through residual strains, for instance.

Alternatively, a structural transition into a twofold symmetric state would naturally explain the observed superconducting anisotropy. No transitions aside from superconductivity have been reported in magnetotransport, calorimetry [62,66,68,83], or recent neutron diffraction measurements on $Cu_xBi_2Se_3$ [45]. Room-temperature synchrotron x-ray diffraction measurements in reflection geometry to high L values along the c^* axis [83] show no distortions from the $R\bar{3}m$ structure. However, Kuntsevich *et al.* [84,85] report a 0.02% monoclinic distortion in the (2 0 5) and (1 1 15) peaks at room temperature in single-crystal $Sr_xBi_2Se_3$. Additionally, Cho *et al.* [86] report distortion of the lattice along one in-plane direction just above T_c via dilatometry measurements, suggesting that the structural distortion could be masked in other bulk probes by the superconducting transition. While it is unlikely that the small reported distortion ($\Delta\ell/\ell \sim 10^{-7}$) could account for the large in-plane superconducting anisotropy of $\Gamma \sim 3-4$ at $T = 0$ [66,83], it may nevertheless pin the nematic axis. Recent theoretical work, though, suggests that any "vestigial" order above T_c may be coincidental or due to broadened superconducting transitions [87].

Here, we present simultaneous resistivity and XRD measurements on a $Sr_{0.1}Bi_2Se_3$ crystal. By monitoring the sample's resistance, we measure the superconducting transition as a function of temperature and apply magnetic field while recording the in-plane Bragg reflections. Our results indicate the absence of any in-plane crystallographic distortion at the level of 1×10^{-5} associated with the superconducting transition. These results further support the model that the large twofold in-plane anisotropy of superconducting properties of $Sr_xBi_2Se_3$ is not structural in origin, but electronic. Namely, it is caused by a nematic superconducting order parameter of E_u symmetry. Our multimodal measurement technique combining simultaneous subkelvin magnetotransport and diffraction measurements on a single crystal at a synchrotron beam line serves as a proof-of-concept experiment which may open new avenues for materials science research.

II. EXPERIMENTAL METHODS

A relatively large ~2 (l) × 0.65 (w) × 0.0125 (h) cm rectangular platelike single crystal was cleaved from a bulk crystal, grown via the melt-growth technique [79]. The crystal was prescreened for superconductivity in a custom-built superconducting quantum interference device (SQUID) magnetometer with a small conventional magnet. Gold electrical contact strips were evaporated onto the long face of the crystal, and 50-μm gold wires were then attached to the strips using silver epoxy in a conventional four-point measurement configuration, with a current flow of 0.1 mA in the a-a^* plane. An AMI 90/10/10 kG superconducting three-axis vector magnet with a standard ^{4}He variable temperature insert was used for magnetotransport measurements before and after the synchrotron characterization. The vector magnet allowed for the magnetic field to be swept in the a-a^* plane in the crystal without having to physically rotate the sample. For the synchrotron measurements, the sample was mounted at one end onto a sapphire wafer with silver epoxy, while the other end extended beyond the sapphire substrate, thereby enabling unobstructed x-ray transmission (see Fig. 1). The sapphire wafer, in turn, was glued with GE 7031 varnish onto the cold stage of the cryostat. With the help of Laue pictures [Fig. 1(b), inset], the sample was aligned such that the a axis was oriented parallel to the cryostat axis. X-ray measurements were performed at the 6-ID-C beam line at the Advanced Photon Source at Argonne National Laboratory with a beam energy of 19.9 keV, sufficiently high to ensure reasonable transmission. Beam slits were positioned such that an illuminated area of approximately 300 × 300 μm was located between the two voltage contacts, as indicated in Fig. 1(b). Transport measurements were performed *in situ* in the x-ray beam in magnetic fields of up to 45 kG generated by a split-coil superconducting magnet affording wide horizontal optical access. The transport wires were anchored at multiple places on the probe and cold-head to minimize heat loading from room temperature to the ^{3}He pot. Currents of 0.1 mA were used in all transport

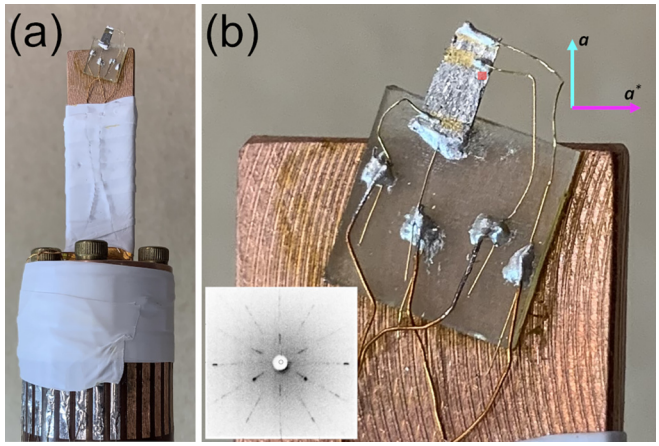

FIG. 1. Single crystal of $Sr_{0.1}Bi_2Se_3$, wired for transport measurements and mounted on a sapphire wafer on the cold stage of a ^{3}He cryostat suitable for transmission x-ray diffraction (XRD). The sample is oriented such that the a axis of the crystal is parallel to the long axis of the probe (and thus parallel to the applied magnetic field). The inset in (b) shows a Laue pattern of the single crystal of $Sr_{0.1}Bi_2Se_3$, used for orienting the sample. The red-shaded area near a voltage contact marks the beam spot.

measurements on the ^{3}He cold finger, and a ramp rate of 0.1 K/min was used at low temperature to measure all $R(T)$ curves. With the sample mounted as shown in Fig. 1, the ^{3}He cold finger thermometer attached to the ^{3}He pot reached a base temperature of 0.68 K with a hold time of approximately 30 minutes, sufficiently long to record x-ray scans.

III. RESULTS AND DISCUSSION

Figure 2(a) shows the temperature dependence of the resistance of the $Sr_{0.1}Bi_2Se_3$ crystal as measured in the AMI vector magnet in zero field. We find a residual resistivity ratio of about 1.45, and a sharp superconducting transition with an onset at approximately 3.0 K and a transition width $\Delta T_c < 0.2$ K, typical for $Sr_{0.1}Bi_2Se_3$ crystals. Figure 2(b) shows the field dependence of the resistance of the crystal at 2.1 K with H ∥ a as measured in the ^{3}He cold finger cryostat at the synchrotron in no beam; in 45 kG, the sample is fully in the normal state.

The resistance of the $Sr_{0.1}Bi_2Se_3$ crystal as a function of in-plane angle in an applied magnetic field of 10 kG in the AMI vector magnet cryostat is shown in Fig. 3 for

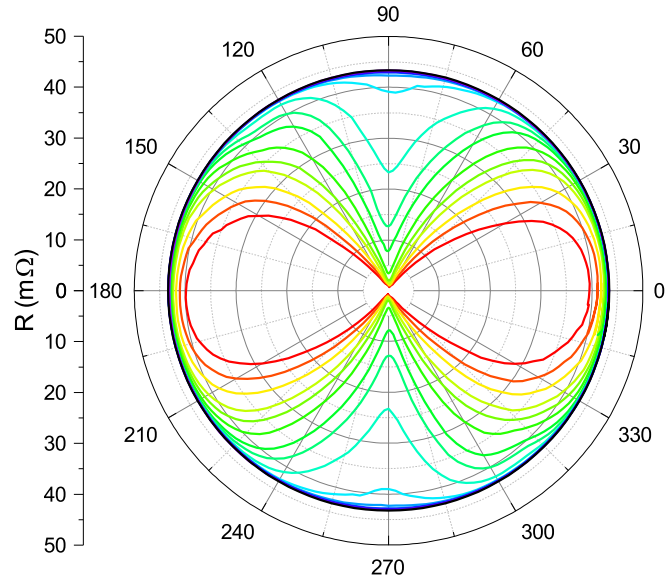

FIG. 3. $R(\theta)$ with $H = 10$ kG swept in the a-a^* plane for the same crystal showing the twofold axis of symmetry, with the high-H_{c2} direction pinned to the a axis (90°). Temperatures start at 1.8 K (innermost, red) and increase in 0.1 K steps until the normal state isotropic behavior is recovered above T_c (outermost, black).

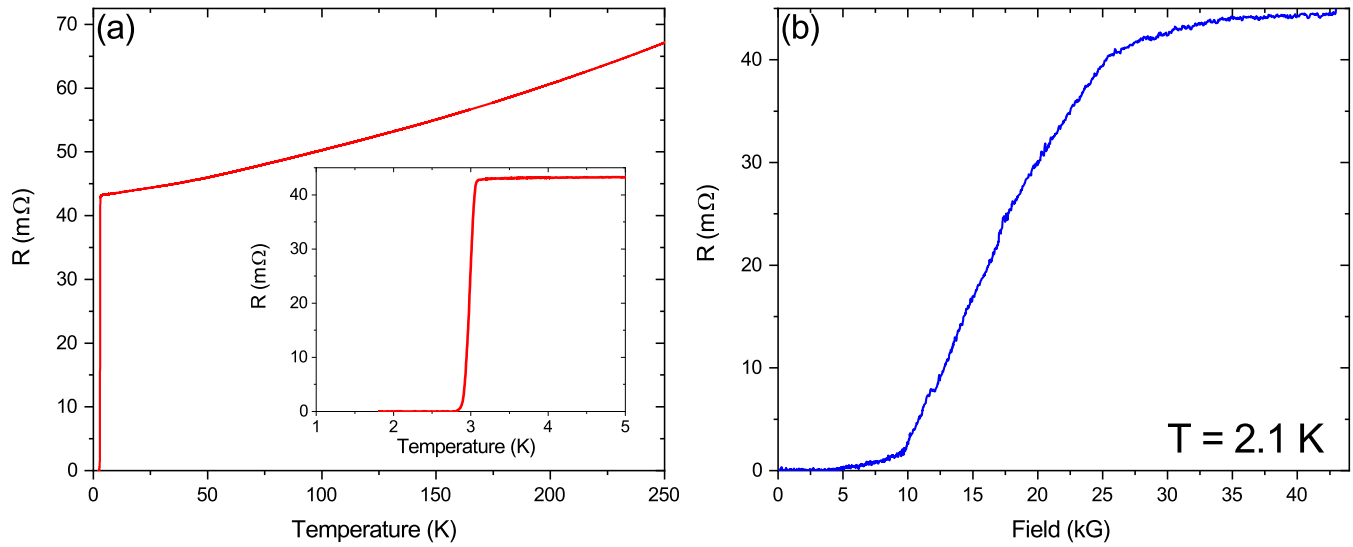

FIG. 2. (a) Resistance vs temperature of the single crystal of $Sr_{0.1}Bi_2Se_3$ selected for synchrotron measurements in zero applied field as measured in a conventional ^{4}He exchange gas cryostat. The inset shows the transition on expanded scales; $T_{c,\text{onset}} \approx 3.0$ K. (b) Resistance at 2.1 K as a function of magnetic field applied along the a axis of the crystal, obtained at the synchrotron cryostat with the x-ray beam off. At 2.1 K, a maximum field of 45 kG is enough to drive the sample into the normal state.

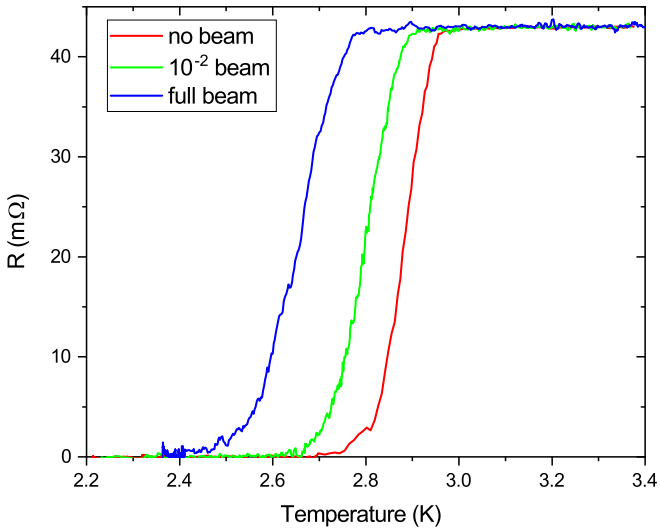

FIG. 4. Resistance vs temperature of the $Sr_{0.1}Bi_2Se_3$ crystal *in situ* on the synchrotron stage demonstrating beam-induced heating. With the full beam (10^{11} γ/sec), the transition is only lowered by ~300 mK.

temperatures from 1.8 K (red) to above T_c (black), in 0.1 K steps. The angular dependence of the resistance shows the characteristic twofold anisotropy of the upper critical field H_{c2} observed in the nematic superconducting state. Directions with lower H_{c2} will be resistive, whereas directions with higher H_{c2} remain superconducting; as temperature increases, the anisotropy lifts. Laue x-ray measurements [inset of Fig. 1(b)] on the same crystal confirm that the high-H_{c2} direction (marked as 90° in Fig. 3) is a crystallographic a axis, consistent with all previous measurements on crystals of $Sr_xBi_2Se_3$ by our group.

A persisting challenge in low-temperature XRD measurements is assessing the "true" sample temperature which, due to beam-induced heating, may be significantly higher than the thermometer reading [88]. In our multimodal setup, we use the temperature dependence of the resistance and the location of the superconducting transition as an indication of the actual sample temperature. Figure 4 shows *in situ* resistance vs temperature measurements under different levels of beam load. With a full beam of approximately 10^{11} γ/sec, the transition is suppressed by only ~300 mK; different beam attenuation levels were seen to shift the superconducting transition temperature between these two extrema. This suggests that around 2 K, beam-induced heating raises the sample temperature by, at most, 0.30 K above the thermometry reading.

However, as the beam footprint is considerably smaller than the sample area [see Fig. 1(b)], colder, that is, superconducting, sections in the sample might effectively short out a resistance measurement in the presence of a substantial temperature increase in the beam spot. In order to address this potential issue, we have performed large-scale simulations of the temperature distribution in our sample by solving the heat diffusion equation until a steady state is reached. To this end, the sample is discretized in a 5-μm-size mesh in all three directions (i.e., 512 × 268 × 25 grid point total). On one end of the sample, an additional small 50 μm piece of silver epoxy is included in the simulation as it attaches to both the sapphire substrate and an electrode. All four electrodes and the sapphire crystal are taken into account as thermal baths (heat sinks) using the related heat conductivities of the contact materials. The beam spot is added as a volumetric heat source. Overall, the geometry of the sample and all heat sources and sinks are faithfully reproduced in the simulation. As there are no measurements of the low-temperature thermal conductivity of $Sr_{0.1}Bi_2Se_3$, we refer to related materials $Cu_xBi_2Se_3$ and Bi_2Se_3 for which values of $\kappa \sim 1-2\,\mathrm{W/(K*m)}$ [89] and $\kappa \sim 15$ W/(K*m) [90], respectively, have been reported. In our simulations, we adopt values of $\kappa \sim 1$ to 2 W/(K*m) and neglect the increase of κ with increasing temperature. The linear absorption coefficient of $Sr_{0.1}Bi_2Se_3$ for x rays with an energy of 20 keV is ~500 cm^{-1} [91], yielding an essentially uniformly absorbed power density of ~1 W/cm^3 in a sample of 125 μm thickness. This value is an upper limit as we do not account for energy removal due to fluorescent x rays and photoelectrons.

We construct an approximate thermal model of our sample assembly [see Fig. 5(a)] which is based on the experimental layout shown in Fig. 1(b). Heat removal from the sample is established via the metallic contacts through the silver epoxy, gold, and copper wires, as well as via the silver epoxy gluing of the sample to the sapphire substrate. As the thermal interface resistances are largely unknown, we explore a range of thermal resistances connecting the sample to the bath temperature subject to the constraint that under beam load, the coldest path between the voltage contacts has a temperature of approximately 0.3 K above bath. Examples of the resulting temperature distributions across and along the sample are shown in Figs. 5(b) and 5(c), defining the x axis as the long side and the y axis as the short side of the crystal. While the temperature distribution is found to be inhomogeneous, in all cases the enhancement of the temperature in the beam spot is limited to, at most, 0.1 K above the remaining sample—across the sample in the y direction, the temperature variation is even less than 0.05 K. Qualitatively, the rather small overheating effects can be accounted for by (a) the reasonably high in-plane thermal conductivity of Bi_2Se_3-materials (on par with brass or aluminum alloys) and (b) the placement of the heat sinks right next to the beam spot and at the far ends of the sample, reducing temperature gradients across the width of the sample. We therefore surmise that the resistivity data shown in Figs. 2(b) and 4 indicate that the sample is in the superconducting state under beam spot.

A monoclinic distortion, as reported by Kuntsevich *et al.* [84,85], should manifest itself as a splitting and/or shift of high-symmetry peaks as the three rotationally symmetric a directions in the nominal $R\bar{3}m$ trigonal structure would no longer be equivalent. Here, we report results on the (300) reflection. Figure 6 shows H-scans in a narrow window centered around $H = 3$ recorded at the base temperature of the system (0.68 K, black) and above T_c (5.3 K, green). There is no discernible difference between the two scans, strongly suggesting that there is no crystallographic transition at or close to T_c, which could be masked by the superconducting signal in measurement techniques such as magnetization, magnetotransport, and calorimetry. Our results are also

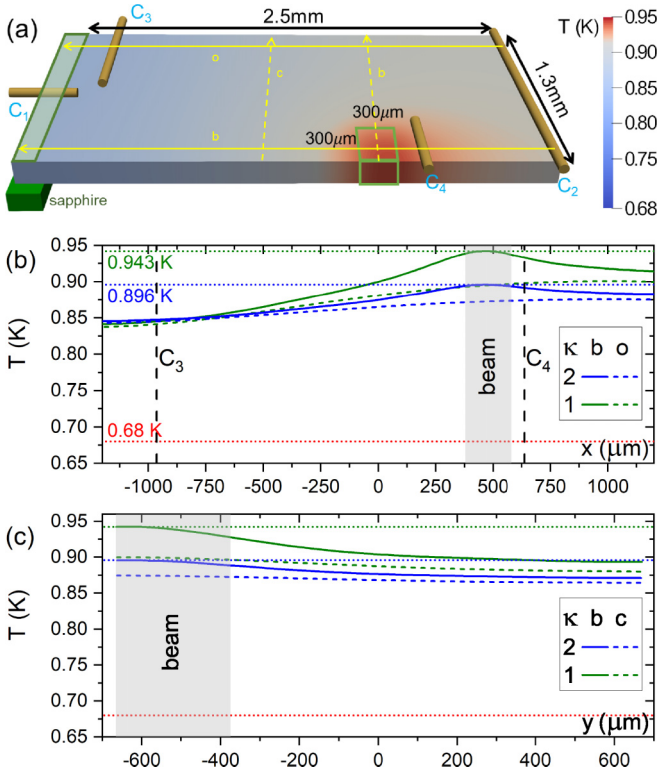

FIG. 5. (a) Steady-state temperature distribution of the SBS sample. The four electrode gold wires are indicated as C_1–C_4, and the sapphire substrate in green. These are modeled as heat sinks using the thermal conductivities of the contact materials. On the left, a 50 μm epoxy region attached to the SBS is also simulated (indicated as shaded-green area). The 300 × 300 μm beam area is outlined in green. The temperature distribution in (a) is obtained for a heat conductivity for the SBS of $\kappa = 1$ W/K*m. (b), (c) The temperature distribution along yellow lines indicating various cuts across the sample (b [beam], c [center], o [opposite]) shown in (a) in the x and y directions, respectively. (b) Temperature profiles in the x direction along cut lines b and o are solid and dashed, respectively, with blue indicating $\kappa = 2$ W/K*m and green indicating $\kappa = 1$ W/K*m. (c) Temperature profiles in the y direction along cut lines b and c are solid and dashed, respectively, with blue indicating $\kappa = 2$ W/K*m and green indicating $\kappa = 1$ W/K*m. In each panel, gray shading indicates the beam area, and dashed vertical black lines indicate electrodes, as marked. Maximum temperatures and bath temperature are indicated by horizontal dashes lines with their kelvin values.

inconsistent with any monoclinic distortion away from the nominal threefold symmetric $R\bar{3}m$ structure.

In addition to varying the sample temperature, the application of a magnetic field allows driving the sample into the normal state while holding the temperature constant. With our sample geometry (Fig. 1), the field was applied along the crystallographic a axis, which is the axis of high H_{c2}. The sample was kept at $T = 2.1$ K, while the field was ramped from 0 to 45 kG. The field was ramped slowly to avoid eddy current heating, and no significant sample stage heater output variations were observed during ramping, suggesting that any field-induced heating or variations in thermometry were negligible. Figure 2(b) shows the field dependence of the sample at 2.1 K with the beam off. The onset of resistance

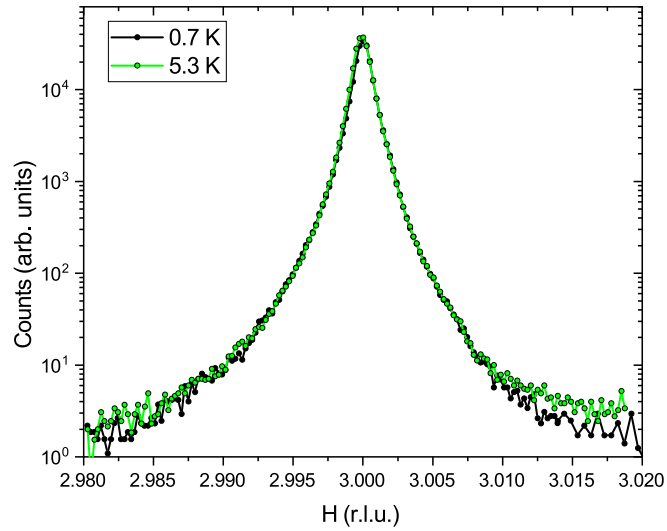

FIG. 6. The (300) peak in the $R\bar{3}m$ structure deep in the superconducting state (0.69 K, black) and above T_c (5.3 K, green). There is no discernible difference, suggesting no symmetry-breaking distortion of the lattice.

occurs around 6 kG, which is consistent with values at 2.1 K for similar crystals. These data demonstrate that the applied magnetic field is able to drive the sample normal while on the cold finger of the beam-line cryostat.

A narrow window in H around the (300) diffraction peak was then scanned at a fixed temperature of 2.1 K in increasing fields from 0 to 40 kG [Fig. 7(a)]. This field range guarantees that the peak is measured on either side of and across the superconducting transition. A Pearson VII fit [92],

$$y = y_0 + A\frac{2\Gamma(m)\sqrt{2^{-m}-1}}{\sqrt{\pi}\Gamma(m-1/2)w} \times \left[1 + 4 * \frac{2^{-m}-1}{w^2}(x-x_c)^2\right]^{-m},$$

was used on each dataset. The panels of Fig. 7(b) show the evolution of the central value of the peak x_c (top), the width parameter w (middle), and the exponent m (bottom); for each, there is essentially no shift as the sample exits the superconducting state. This suggests that there is no crystallographic shift or distortion associated with the superconducting transition. The uncertainties of the fit parameters x_c, w, and m are 4×10^{-5}, 6×10^{-6}, and 7×10^{-2}, respectively, slightly increasing with increasing applied field. Importantly, the observed variations are random. In particular, there is no uniform trend, for instance towards increased x_c or w with increasing magnetic field. We therefore conclude that the data shown in Figs. 7(a) and 7(b) indicate that there is no in-plane crystallographic distortion at the level of 1×10^{-5} associated with the superconducting transition. These results further support the model that the large twofold in-plane anisotropy of superconducting properties of $Sr_xBi_2Sr_3$ is electronic in origin, namely, caused by the nematic superconducting order parameter of E_u symmetry.

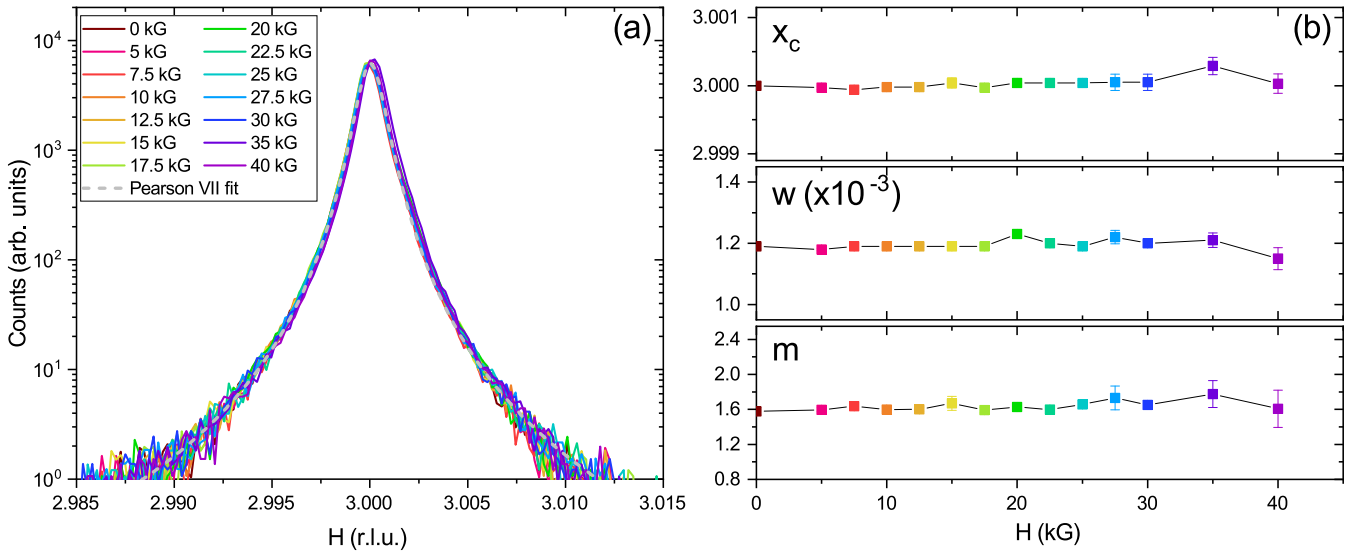

FIG. 7. (a) The (300) peak in the $R\bar{3}m$ structure at 2.1 K as a function of applied field. As the field increases, the sample exits the superconducting state, but no change in the (300) peak is observed. (b) Pearson-VII fit parameters x_c (top), w (middle), m (bottom) as a function of field.

IV. CONCLUSION

Our experiments demonstrate the viability of subkelvin synchrotron diffraction measurements. We estimate that the sample reached a temperature under 1 K with a full beam of approximately 10^{11} γ/sec at an energy of 19.9 keV, and a base temperature of approximately 0.68 K with no beam. By monitoring the resistance, we demonstrated that the $Sr_{0.1}Bi_2Se_3$ sample remains superconducting in-beam, verifying that our base temperature diffraction measurements were performed deep in the superconducting state. Numerical solutions of the heat diffusion equation show that while there is an inhomogeneous temperature distribution due to beam heating, the entire sample transitions into the superconducting state. We saw no difference between the high-symmetry (300) peaks at the base temperature of $\sim 0.25T_c$ and at $\sim 1.5T_c$, and we saw no change in the (300) peak as the sample was driven into the normal state with an applied magnetic field. Our results indicate that there is no in-plane crystallographic distortion of the average lattice structure at the level of 1×10^{-5} associated with the superconducting transition. While our XRD measurements do not reach the resolution of 10^{-7} reported in recent low-temperature dilatometry experiments [86], our results further support the model in which the large twofold in-plane anisotropy of the superconducting properties of $Sr_xBi_2Sr_3$ is not structural in origin but electronic, namely, it is caused by a nematic superconducting order parameter of E_u symmetry. The multimodal measurement capability has proven essential for quantifying beam-induced sample heating which, in the present case, amounted to about 0.30 K.

ACKNOWLEDGMENTS

Work at Argonne National Laboratory was supported by the U.S. Department of Energy, Office of Science, Basic Energy Sciences, Materials Sciences and Engineering Division. This research used resources of the APS, a U.S. DOE Scientific User Facility, operated for the DOE Office of Science by Argonne National Laboratory under Contract No. DE-AC02-06CH11357. Work at Brookhaven National Laboratory was supported by the Office of Basic Energy Sciences, Division of Materials Sciences and Engineering, U.S. Department of Energy under Contract No. DE-SC00112704.

[1] L. Fu, C. L. Kane, and E. J. Mele, Topological insulators in three dimensions, Phys. Rev. Lett. **98**, 106803 (2007).

[2] H. Zhang, C.-X. Liu, X.-L. Qi, X. Dai, Z. Fang, and S.-C. Zhang, Topological insulators in Bi_2Se_3, Bi_2Te_3 and Sb_2Te_3 with a single Dirac cone on the surface, Nat. Phys. **5**, 438 (2009).

[3] Y. Xia, D. Qian, D. Hsieh, L. Wray, A. Pal, H. Lin, A. Bansil, D. Grauer, Y. S. Hor, R. J. Cava, and M. Z. Hasan, Observation of a large-gap topological-insulator class with a single Dirac cone on the surface, Nat. Phys. **5**, 398 (2009).

[4] D. Hsieh, Y. Xia, D. Qian, L. Wray, J. H. Dil, F. Meier, J. Osterwalder, L. Patthey, J. G. Checkelsky, N. P. Ong, A. V. Fedorov, H. Lin, A. Bansil, D. Grauer, Y. S. Hor, R. J. Cava, and M. Z. Hasan, A tunable topological insulator in the spin helical Dirac transport regime, Nature (London) **460**, 1101 (2009).

[5] K. Mazumder and P. M. Shirage, A brief review of Bi_2Se_3 based topological insulator: From fundamentals to applications, J. Alloys Compd. **888**, 161492 (2021).

[6] L. Fu and C. L. Kane, Superconducting proximity effect and Majorana fermions at the surface of a topological insulator, Phys. Rev. Lett. **100**, 096407 (2008).

[7] A. P. Schnyder, S. Ryu, A. Furusaki, and A. W. W. Ludwig, Classification of topological insulators and superconductors in three spatial dimensions, Phys. Rev. B **78**, 195125 (2008).

[8] X.-L. Qi, T. L. Hughes, S. Raghu, and S.-C. Zhang, Time-reversal-invariant topological superconductors and superfluids in two and three dimensions, Phys. Rev. Lett. **102**, 187001 (2009).

[9] M. Z. Hasan and C. L. Kane, *Colloquium*: Topological insulators, Rev. Mod. Phys. **82**, 3045 (2010).

[10] X. L. Qi and S.-C. Zhang, Topological insulators and superconductors, Rev. Mod. Phys. **83**, 1057 (2011).

[11] Y. Tanaka, M. Sato, and N. Nagaosa, Symmetry and topology in superconductors - Odd-frequency pairing and edge states, J. Phys. Soc. Jpn. **81**, 011013 (2012).

[12] S. Sasaki and T. Mizushima, Superconducting doped topological materials, Physica C **514**, 206 (2015).

[13] M. Z. Hasan, S.-Y. Xu, and G. Bian, Topological insulators, topological superconductors and Weyl fermion semimetals: discoveries, perspectives and outlooks, Phys. Scr. **T168**, 019501 (2016).

[14] T. Mizushima, Y. Tsutsumi, T. Kawakami, M. Sato, M. Ichioka, and K. Machida, Symmetry-protected topological superfluids and superconductors - From the basics to ^{3}He, J. Phys. Soc. Jpn. **85**, 022001 (2016).

[15] A. P. Schnyder and P. M. R. Brydon, Topological surface states in nodal superconductors, J. Phys.: Condens. Matter **27**, 243201 (2015).

[16] F. Wilczek, Majorana returns, Nat. Phys. **5**, 614 (2009).

[17] A. R. Akhmerov, J. Nilsson, and C. W. J. Beenakker, Electrically detected interferometry of Majorana fermions in a topological insulator, Phys. Rev. Lett. **102**, 216404 (2009).

[18] M. Leijnse and K. Flensberg, Introduction to topological superconductivity and Majorana fermions, Semicond. Sci. Technol. **27**, 124003 (2012).

[19] V. Mourik, K. Zuo, S. M. Frolov, S. R. Plissard, E. P. A. M. Bakkers, and L. P. Kouwenhoven, Signatures of Majorana fermions in hybrid superconductor-semiconductor nanowire devices, Science **336**, 1003 (2012).

[20] A. Das, Y. Ronen, Y. Most, Y. Oreg, M. Heiblum, and H. Shtrikman, Zero-bias peaks and splitting in an Al–InAs nanowire topological superconductor as a signature of Majorana fermions, Nat. Phys. **8**, 887 (2012).

[21] L. P. Rokhinson, X. Liu, and J. K. Furdyna, The fractional ac Josephson effect in a semiconductor-superconductor nanowire as a signature of Majorana particles, Nat. Phys. **8**, 795 (2012).

[22] C. W. J. Beenakker, Search for Majorana fermions in superconductors, Annu. Rev. Condens. Matter Phys. **4**, 113 (2013).

[23] S. M. Albrecht, A. P. Higginbotham, M. Madsen, F. Kuemmeth, T. S. Jespersen, J. Nygard, P. Krogstrup, and C. M. Marcus, Exponential protection of zero modes in Majorana islands, Nature (London) **531**, 206 (2016).

[24] A. S. Erickson, J.-H. Chu, M. F. Toney, T. H. Geballe, and I. R. Fisher, Enhanced superconducting pairing interaction in indium-doped tin telluride, Phys. Rev. B **79**, 024520 (2009).

[25] Y. S. Hor, A. J. Williams, J. G. Checkelsky, P. Roushan, J. Seo, Q. Xu, H. W. Zandbergen, A. Yazdani, N. P. Ong, and R. J. Cava, Superconductivity in $Cu_xBi_2Se_3$ and its implications for pairing in the undoped topological insulator, Phys. Rev. Lett. **104**, 057001 (2010).

[26] S. Sasaki, Z. Ren, A. A. Taskin, K. Segawa, L. Fu, and Y. Ando, Odd-parity pairing and topological superconductivity in a strongly spin-orbit coupled semiconductor, Phys. Rev. Lett. **109**, 217004 (2012).

[27] R. D. Zhong, J. A. Schneeloch, T. S. Liu, F. E. Camino, J. M. Tranquada, and G. D. Gu, Superconductivity induced by In substitution into the topological crystalline insulator $Pb_{0.5}Sn_{0.5}Te$, Phys. Rev. B **90**, 020505(R) (2014).

[28] C. M. Polley, V. Jovic, T.-Y. Su, M. Saghir, D. Newby, B. J. Kowalski, R. Jakiela, A. Barcz, M. Guziewicz, T. Balasubramanian, G. Balakrishnan, J. Laverock, and K. E. Smith, Observation of surface states on heavily indium-doped SnTe(111), a superconducting topological crystalline insulator, Phys. Rev. B **93**, 075132 (2016).

[29] H. Zhang, C.-X. Liu, S. Gazibegovic, D. Xu, J. A. Logan, G. Wang, N. van Loo, J. D. S. Bommer, M. W. A. de Moor, D. Car, R. L. M. Op het Veld, P. J. van Veldhoven, S. Koelling, M. A. Verheijen, M. Pendharkar, D. J. Pennachio, B. Shojaei, J. S. Lee, C. J. Palmstrøm, E. P. A. M. Bakkers, S. Das Sarma, and L. P. Kouwehoven, Retraction note: Quantized Majorana conductance, Nature (London) **591**, E30 (2021).

[30] D. Castelvecchi, Evidence of elusive Majorana particle dies—but computing hope lives on, Nature (London) **591**, 354 (2021).

[31] Y. Qiu, K. N. Sanders, J. Dai, J. E. Medvedeva, W. Wu, P. Ghaemi, T. Vojta, and Y. S. Hor, Time reversal symmetry breaking superconductivity in topological materials, arXiv:1512.03519.

[32] Z. Liu, X. Yao, J. Shao, M. Zuo, L. Pi, S. Tan, C. Zhang, and Y. Zhang, Superconductivity with topological surface state in $Sr_xBi_2Se_3$, J. Am. Chem. Soc. **137**, 10512 (2015).

[33] L. A. Wray, S.-Y. Xu, Y. Xia, Y. S. Hor, D. Qian, A. V. Fedorov, H. Lin, A. Bansil, R. J. Cava, and M. Z. Hasan, Observation of topological order in a superconducting doped topological insulator, Nat. Phys. **6**, 855 (2010).

[34] J. Zich, M. Misek, V. Holy, K. Carva, J. Cizek, J. Navratil, P. Cermak, P. Knotek, K. Sraitrova, S. Cichon, J. Hejtmanek, Z. Jirak, and C. Drasar, $Fe_xBi_2Se_3$ superconductivity, dimensional transport, and high electron mobility are associated with the natural nanostructure of Bi_2Se_3 single crystals, Phys. Rev. B **108**, 125308 (2023).

[35] N. Levy, T. Zhang, J. Ha, F. Sharifi, A. A. Talin, Y. Kuk, and J. A. Stroscio, Experimental evidence for *s*-wave pairing symmetry in superconducting $Cu_xBi_2Se_3$ single crystals using a scanning tunneling microscope, Phys. Rev. Lett. **110**, 117001 (2013).

[36] M. Kriener, K. Segawa, Z. Ren, S. Sasaki, S. Wada, S. Kuwabata, and Y. Ando, Electrochemical synthesis and superconducting phase diagram of $Cu_xBi_2Se_3$, Phys. Rev. B **84**, 054513 (2011).

[37] R. Kondo, T. Yoshinaka, Y. Imai, and A. Maeda, Reproducible synthetic method for the topological superconductor $Cu_xBi_2Se_3$, J. Phys. Soc. Jpn. **82**, 063702 (2013).

[38] M. Wang, Y. Song, L. You, Z. Li, B. Gao, X. Xie, and M. Jiang, A combined method for synthesis of superconducting Cu doped Bi_2Se_3, Sci. Rep. **6**, 22713 (2016).

[39] K. Kobayashi, T. Ueno, H. Fujiwara, T. Yokoya, and J. Akimitsu, Unusual upper critical field behavior in Nb-doped bismuth selenides, Phys. Rev. B **95**, 180503(R) (2017).

[40] J. Wang, F. Jiao, D. Zhang, M. Chang, L. Cai, Y. Li, C. Wang, S. Tan, Q. Jing, B. Liu, and D. Qian, Investigate the Nb doping position and its relationship with bulk topological superconductivity in $Nb_xBi_2Se_3$ by X-ray photoelectron spectra, J. Phys. Chem. Solids **137**, 109208 (2020).

[41] M. E. Kamminga, M. Batuk, J. Hadermann, and S. J. Clarke, Misfit phase $(BiSe)_{1.10}NbSe_2$ as the origin of superconductivity in niobium-doped bismuth selenide, Commun. Mater. **1**, 82 (2020).

[42] S. M. Kevy, H. E. Lund, L. Wollesen, K. J. Dalgaard, Y.-T. Hsu, S. Wiedmann, M. Bianchi, Ann Julie Utne Holt, D. Curcio, D. Biswas, A. J. H. Jones, K. Volckaert, C. Cacho, P. Dudin, P. Hofmann, and M. Bremholm, Structural and electronic inhomogeneity of superconducting Nb-doped Bi_2Se_3, Phys. Rev. B **103**, 085107 (2021).

[43] K. J. Dalgaard, S. M. Kevy, L. Wollesen, Q. Ma, S. Wiedmann, Kajsa G. V. Sigfridsson Clauss, and M. Bremholm, Local structure of Nb in superconducting Nb-doped Bi_2Se_3, Phys. Rev. B **103**, 184103 (2021).

[44] S. M. Kevy, L. Wollesen, K. J. Dalgaard, Y.-T. Hsu, S. Wiedmann, and M. Bremholm, Large variation in superconducting transition temperature in the $Nb_xBi_{2-x}Se_3$ system, Phys. Rev. Mater. **8**, 054801 (2024).

[45] T. Frøhlich, Z. Wang, M. Bagchi, A. Stunault, Y. Ando, and M. Braden, Crystal structure and distortion of superconducting $Cu_xBi_2Se_3$, Phys. Rev. Mater. **4**, 054802 (2020).

[46] Z. Li, M. Wang, D. Zhang, N. Feng, W. Jiang, C. Han, W. Chen, M. Ye, C. Gao, J. Jia, J. Li, S. Qiao, D. Qian, B. Xu, H. Tian, and B. Gao, Possible structural origin of superconductivity in Sr-doped Bi_2Se_3, Phys. Rev. Mater. **2**, 014201 (2018).

[47] S.-H. Yu, T. L. Hung, M.-N. Ou, M. M. C. Chou, and Y.-Y. Chen, Zero Cu valence and superconductivity in high-quality $Cu_xBi_2Se_3$ crystal, Phys. Rev. B **100**, 174502 (2019).

[48] Y.-R. Lin, M. Bagchi, S. Soubatch, T.-L. Lee, J. Brede, F. C. Bocquet, C. Kumpf, Y. Ando, and F. S. Tautz, Vertical position of Sr dopants in the $Sr_xBi_2Se_3$ superconductor, Phys. Rev. B **104**, 054506 (2021).

[49] S. M. Kevy, L. Wollesen, and M. Bremholm, In-situ x-ray diffraction study of Nb-doped Bi_2Se_3 crystal growth revealing unavoidable misfit layer compound, J. Solid State Chem. **330**, 124477 (2024).

[50] A. Sirohi, S. Das, P. Neha, K. S. Jat, S. Patnaik, and G. Sheet, Low-energy excitations and non-BCS superconductivity in Nb_x - Bi_2Se_3, Phys. Rev. B **98**, 094523 (2018).

[51] B. J. Lawson, P. Corbae, G. Li, F. Yu, T. Asaba, C. Tinsman, Y. Qiu, J. E. Medvedeva, Y. S. Hor, and L. Li, Multiple Fermi surfaces in superconducting Nb-doped Bi_2Se_3, Phys. Rev. B **94**, 041114(R) (2016).

[52] M. P. Smylie, H. Claus, U. Welp, W.-K. Kwok, Y. Qiu, Y. S. Hor, and A. Snezhko, Evidence of nodes in the order parameter of the superconducting doped topological insulator $Nb_xBi_2Se_3$ via penetration depth measurements, Phys. Rev. B **94**, 180510(R) (2016).

[53] M. P. Smylie, K. Willa, H. Claus, A. Snezhko, I. Martin, W.-K. Kwok, Y. Qiu, Y. S. Hor, E. Bokari, P. Niraula, A. Kayani, V. Mishra, and U. Welp, Robust odd-parity superconductivity in the doped topological insulator $Nb_xBi_2Se_3$, Phys. Rev. B **96**, 115145 (2017).

[54] Shruti, V. K. Maurya, P. Neha, P. Srivastava, and S. Patnaik, Superconductivity by Sr intercalation in the layered topological insulator Bi_2Se_3, Phys. Rev. B **92**, 020506(R) (2015).

[55] C. Q. Han, H. Li, W. J. Chen, F. Zhu, M.-Y. Yaho, Z. J. Li, M. Wang, B. F. Gao, D. D. Guan, C. Liu, C. L. Gao, D. Qian, and J.-F. Jia, Electronic structure of a superconducting topological insulator Sr-doped Bi_2Se_3, Appl. Phys. Lett. **107**, 171602 (2015).

[56] G. Du, J. Shao, X. Yang, Z. Du, D. Fang, J. Wang, K. Ran, J. Wen, C. Zhang, H. Yang, Y. Zhang, and H.-H. Wen, Drive the Dirac electrons into Cooper pairs in $Sr_xBi_2Se_3$, Nat. Commun. **8**, 14466 (2017).

[57] B. J. Lawson, Y. S. Hor, and L. Li, Quantum oscillations in the topological superconductor candidate $Cu_{0.25}Bi_2Se_3$, Phys. Rev. Lett. **109**, 226406 (2012).

[58] B. J. Lawson, G. Li, F. Yu, T. Asaba, C. Tinsman, T. Gao, W. Wang, Y. S. Hor, and L. Li, Quantum oscillations in $Cu_xBi_2Se_3$ in high magnetic fields, Phys. Rev. B **90**, 195141 (2014).

[59] E. Lahoud, E. Maniv, M. S. Petrushevsky, M. Naamneh, A. Ribak, S. Wiedmann, L. Petaccia, Z. Salman, K. B. Chashka, Y. Dagan, and A. Kanigel, Evolution of the Fermi surface of a doped topological insulator with carrier concentration, Phys. Rev. B **88**, 195107 (2013).

[60] A. Almoalem, I. Silber, S. Sandik, M. Lotem, A. Ribak, Y. Nitzav, A. Yu. Kuntsevich, O. A. Sobolevskiy, Y. G. Selivanov, V. A. Prudkoglyad, M. Shi, L. Petaccia, M. Goldstein, Y. Dagan, and A. Kanigel, Link between superconductivity and a Lifshitz transition in intercalated Bi_2Se_3, Phys. Rev. B **103**, 174518 (2021).

[61] R. S. Akzyanov, Lifshitz transition in dirty doped topological insulator with nematic superconductivity, Phys. Rev. B **104**, 224502 (2021).

[62] S. Yonezawa, Nematic superconductivity in doped Bi_2Se_3 topological superconductors, Condensed Matter **4**, 2 (2019).

[63] K. Matano, M. Kriener, K. Segawa, Y. Ando, and G.-Q. Zheng, Spin-rotation symmetry breaking in the superconducting state of $Cu_xBi_2Se_3$, Nat. Phys. **12**, 852 (2016).

[64] L. Fu, Odd-parity topological superconductor with nematic order: Application to $Cu_xBi_2Se_3$, Phys. Rev. B **90**, 100509(R) (2014).

[65] S. Yonezawa, K. Tajiri, S. Nakata, Y. Nagai, Z. Wang, K. Segawa, Y. Ando, and Y. Maeno, Thermodynamic evidence for nematic superconductivity in $Cu_xBi_2Se_3$, Nat. Phys. **13**, 123 (2017).

[66] Y. Pan, A. M. Nikitin, G. K. Araizi, Y. K. Huang, Y. Matsushita, T. Naka, and A. de Visser, Rotational symmetry breaking in the topological superconductor $Sr_xBi_2Se_3$ probed by upper-critical field experiments, Sci. Rep. **6**, 28632 (2016).

[67] T. Asaba, B. J. Lawson, C. Tinsman, L. Chen, P. Corbae, G. Li, Y. Qiu, Y. S. Hor, L. Fu, and L. Li, Rotational symmetry breaking in a trigonal superconductor Nb-doped Bi_2Se_3, Phys. Rev. X **7**, 011009 (2017).

[68] K. Willa, R. Willa, K. W. Song, G. D. Gu, J. A. Schneeloch, R. Zhong, A. E. Koshelev, W.-K. Kwok, and U. Welp, Nanocalorimetric evidence for nematic superconductivity in the doped topological insulator $Sr_{0.1}Bi_2Se_3$, Phys. Rev. B **98**, 184509 (2018).

[69] Y. Sun, S. Kittaka, T. Sakakibara, K. Machida, J. Wang, J. Wen, X. Xing, Z. Shi, and T. Tamegai, Quasiparticle evidence for the nematic state above T_c in $Sr_xBi_2Se_3$, Phys. Rev. Lett. **123**, 027002 (2019).

[70] R. Tao, Y.-J. Yan, X. Liu, Z.-W. Wang, Y. Ando, Q.-H. Wang, T. Zhang, and D.-L. Feng, Direct visualization of the nematic superconductivity in $Cu_xBi_2Se_3$, Phys. Rev. X **8**, 041024 (2018).

[71] J. W. F. Venderbos, V. Kozii, and L. Fu, Odd-parity superconductors with two-component order parameters: Nematic and

chiral, full gap, and Majorana node, Phys. Rev. B **94**, 180504(R) (2016).

[72] S. Sasaki, M. Kriener, K. Segawa, K. Yada, Y. Tanaka, M. Sato, and Y. Ando, Topological superconductivity in $Cu_xBi_2Se_3$, Phys. Rev. Lett. **107**, 217001 (2011).

[73] T. Kirzhner, E. Lahoud, K. B. Chaska, Z. Salman, and A. Kanigel, Point-contact spectroscopy of $Cu_{0.2}Bi_2Se_3$ single crystals, Phys. Rev. B **86**, 064517 (2012).

[74] C. Kurter, A. D. K. Finck, E. D. Huemiller, J. Medvedeva, A. Weis, J. M. Atkinson, Y. Qiu, L. Shen, S. H. Lee, T. Vojta, P. Ghaemi, Y. S. Hor, and D. J. Van Harlingen, Conductance spectroscopy of exfoliated thin flakes of $Nb_xBi_2Se_3$, Nano Lett. **19**, 38 (2019).

[75] Y. Nagai, Robust superconductivity with nodes in the superconducting topological insulator $Cu_xBi_2Se_3$: Zeeman orbital field and nonmagnetic impurities, Phys. Rev. B **91**, 060502(R) (2015).

[76] L. Andersen, A. Ramires, Z. Wang, T. Lorenz, and Y. Ando, Generalized Anderson's theorem for superconductors derived from topological insulators, Sci. Adv. **6**, 9 (2020).

[77] D. C. Cavanagh and P. M. R. Brydon, General theory of robustness against disorder in multiband superconductors, Phys. Rev. B **104**, 014503 (2021).

[78] T. Kawai, C. G. Wang, Y. Kandori, Y. Honoki, K. Matano, T. Kambe, and G.-Q. Zheng, Direction and symmetry transition of the vector order parameter in topological superconductors $Cu_xBi_2Se_3$, Nat. Commun. **11**, 235 (2020).

[79] G. Du, Y. F. Li, J. Schneeloch, R. D. Zhong, G. D. Gu, H. Yang, H. Lin, and H.-H. Wen, Superconductivity with twofold symmetry in topological superconductor $Sr_xBi_2Se_3$, Sci. China PMA **60**, 037411 (2017).

[80] I. Kostylev, S. Yonezawa, Z. Wang, Y. Ando, and Y. Maeno, Uniaxial-strain control of nematic superconductivity in $Sr_xBi_2Se_3$, Nat. Commun. **11**, 4152 (2020).

[81] R. S. Akzyanov, D. A. Khokhlov, and A. L. Rakhmanov, Nematic superconductivity in topological insulators induced by hexagonal warping, Phys. Rev. B **102**, 094511 (2020).

[82] P. T. How and S. K. Yip, Signatures of nematic superconductivity in doped Bi_2Se_3 under applied stress, Phys. Rev. B **100**, 134508 (2019).

[83] M. P. Smylie, K. Willa, H. Claus, A. E. Koshelev, K. W. Song, W.-K. Kwok, Z. Islam, G. D. Gu, J. A. Schneeloch, R. D. Zhong, and U. Welp, Superconducting and normal-state anisotropy of the doped topological insulator $Sr_{0.1}Bi_2Se_3$, Sci. Rep. **8**, 7666 (2018).

[84] A. Yu. Kuntsevich, M. A. Bryzgalov, V. A. Prudkoglyad, V. P. Martovitskii, Yu. G. Selivanov, and E. G. Chizhevskii, Structural distortion behind the nematic superconductivity in $Sr_xBi_2Se_3$, New J. Phys. **20**, 103022 (2018).

[85] A. Yu. Kuntsevich, M. A. Bryzgalov, R. S. Akzyanov, V. P. Martovitskii, A. L. Rakhmanov, and Yu. G. Selivanov, Strain-driven nematicity of odd-parity superconductivity in $Sr_xBi_2Se_3$, Phys. Rev. B **100**, 224509 (2019).

[86] C.-W. Cho, J. Shen, J. Lyu, O. Atanov, Q. Chen, S. H. Lee, Y. S. Hor, D. J. Gawryluk, E. Pomjakushina, M. Bartkowiak, M. Hecker, J. Schmalian, and R. Lortz, Z_3-vestigial nematic order due to superconducting fluctuations in the doped topological insulators $Nb_xBi_2Se_3$ and $Cu_xBi_2Se_3$, Nat. Commun. **11**, 3056 (2020).

[87] P. T. How and S. K. Yip, Absence of Ginzburg-Landau mechanism for vestigial order in the normal phase above a two-component superconductor, Phys. Rev. B **107**, 104514 (2023).

[88] K. Willa, Z. Diao, D. Campanini, U. Welp, R. Divan, M. Hudl, Z. Islam, W. K. Kwok, and A. Rydh, Nanocalorimeter platform for in situ specific heat measurements and x-ray diffraction at low temperature, Rev. Sci. Instrum. **88**, 125108 (2017).

[89] P. A. Lopez, F. Morales Leal, and R. Escudero Derat, Structural and electronic characterization of $Cu_xBi_2Se_3$, J. Mex. Chem. Soc. **60**, 101 (2016).

[90] J. Navratil, J. Horak, T. Plechacek, S. Kamba, P. Lostak, J. S. Dyck, W. Chen, and C. Uher, Conduction band splitting and transport properties of Bi_2Se_3, J. Solid State Chem. **177**, 1704 (2004).

[91] https://physics.nist.gov/PhysRefData/FFast/html/form.html.

[92] M. M. Hall Jr., V. G. Veeraraghavan, H. Rubin, and P. G. Winchell, The approximation of symmetric X-ray peaks by Pearson type VII distributions, J. Appl. Cryst. **10**, 66 (1977).